

## Stable Low-current Electrodeposition of $\alpha$ -MnO<sub>2</sub> on Super-aligned Electrospun Carbon Nanofibers for High-performance Energy Storage

By: Yiyang Liu, Zheng Zeng, Brian Bloom, David H. Waldeck, and [Jianjun Wei](#)

**This is the peer reviewed version of the following article:**

Y. Liu, Z. Zeng, B. Bloom, D. Waldeck, J. Wei, Stable Low-current Electrodeposition of  $\alpha$ -MnO<sub>2</sub> on Super-aligned Electrospun Carbon Nanofibers for High-performance Energy Storage, *Small* **2017** 14 (3), 1703237. DOI: 10.1002/sml.201703237.

**which has been published in final form at <https://doi.org/10.1002/sml.201703237>. This article may be used for non-commercial purposes in accordance with [Wiley Terms and Conditions for Self-Archiving](#).**

**\*\*\*© 2017 WILEY-VCH Verlag GmbH & Co. KGaA, Weinheim. Reprinted with permission. No further reproduction is authorized without written permission from Wiley. This version of the document is not the version of record. \*\*\***

### **Abstract:**

Metal oxide/carbonaceous nanomaterials are promising candidates for energy-storage applications. However, inhomogeneous mass and charge transfer across the electrode/electrolyte interface due to unstable metal oxide/carbonaceous nanomaterial synthesis limit their performance in supercapacitors. Here, it is shown that the above problems can be mitigated through stable low-current electrodeposition of MnO<sub>2</sub> on superaligned electrospun carbon nanofibers (ECNFs). The key to this approach is coupling a self-designed four steel poles collector for aligned ECNFs and a constant low-current (40  $\mu$ A) electrodeposition technique to form a uniform Na<sup>+</sup>-induced  $\alpha$ -MnO<sub>2</sub> film which proceeds by a time-dependent growth mechanism involving cluster-“kebab” structures and ending with a compact, uniform MnO<sub>2</sub> film for high-performance energy storage.

**Keywords:** electrodeposition | electrospun carbon nanofibers | growth mechanisms | MnO<sub>2</sub> | supercapacitors

### **Article:**

Because of the importance of their structure in determining the chemical and electrochemical properties, architectural control of metal oxides in the nano- and microscale regime is an important goal in materials science.<sup>1-3</sup> Metal oxides are essential electrode materials in lithium ion batteries<sup>4-6</sup> and pseudocapacitors/supercapacitors,<sup>7, 8</sup> and the study of their stable synthesis and growth mechanism can lead to better strategies for improving their electrochemical performance in specific capacitance, energy density, and lifecycle stability.<sup>9, 10</sup>

Manganese dioxide (MnO<sub>2</sub>) has been demonstrated to be one of the most promising electrode materials for lithium batteries and pseudocapacitors/supercapacitors, with a theoretical specific

capacitance of  $1370 \text{ F g}^{-1}$ ,<sup>1</sup> ecofriendly properties, and abundant earth reserves.<sup>11</sup> However,  $\text{MnO}_2$  electrodes often suffer from poor electronic and ionic conductivities which can lower their galvanic charge–discharge capacity.<sup>4, 12</sup> In contrast, carbon-based nanomaterials, e.g., carbon nanotubes (CNTs), graphene,<sup>13</sup> and carbon nanofibers (CNFs), can display high electrical conductivity, high charge transfer capability, large specific surface area mesoporosity, and high electrolyte accessibility.<sup>14</sup> In the past decade, a series of carbon nanomaterials (CNT,<sup>15-19</sup> CNT-forest (CNTF),<sup>20</sup> reduced graphene oxide,<sup>21-23</sup> templated graphene foam,<sup>24-26</sup> CNFs<sup>27</sup>) have been coupled with  $\text{MnO}_2$  to lower their electrical resistance while retaining high charge capacity. Among these, CNTF and CNFs have shown great potential in energy-storage applications when optimized to provide a conductive network and maintain mechanical strength.<sup>28</sup> While a number of studies report on well-aligned  $\text{MnO}_2/\text{CNT}$  and  $\text{MnO}_2/\text{CNFs}$  with different morphologies and crystal structures, rarely do they address the mechanism of the  $\text{MnO}_2$  crystal formation during the electrode preparation. In 2008, the fabrication of  $\text{MnO}_x$  nanoflowers on CNT arrays (CNTAs) using techniques of chemical vapor deposition and electrodeposition was reported.<sup>29</sup> This study showed that  $\text{MnO}_x$  nucleated at the junctions of CNTAs, rather than at the curved surfaces, during electrodeposition and demonstrated a strategy for forming  $\text{MnO}_2$  on an aligned structure for high-capacity electrochemical energy-storage devices. The mass loading of metal oxides on CNTAs is, however, limited and the synthesis of CNTAs is time consuming and costly.

CNFs are well known for their inexpensive production, freestanding nature, large porosity, and high conductivity as electrode materials for supercapacitor applications. Electrospinning, which uses electric force to draw charged threads of polymer solutions or polymer melts into nanofibers, has become an efficient fiber production method for creating porous electrospun CNFs (ECNFs) with a subsequent carbonization.<sup>30, 31</sup> Aligned ECNF structures can be used as scaffolds to uniformly support metal oxide nanoarchitectures because their alignment can significantly enhance the deposition rate by shortening the distance of electron transport.

We hypothesize that the combination of these two materials ( $\text{MnO}_2$  and superaligned ECNFs) in a nanoscale structure will exhibit excellent electrical, electrochemical, and mechanical properties for electrochemical energy storage. In this study, we describe the rational design and fabrication of  $\text{MnO}_2/\text{ECNFs}$  by wrapping  $\text{MnO}_2$  onto superaligned ECNFs. The low-current electrodeposition of the  $\alpha\text{-MnO}_2$  film can be described by a three-stage growth process. The as-prepared  $\text{MnO}_2/\text{ECNFs}$  (formed by a 4 h electrodeposition) electrode exhibits a high capacitance of  $630 \text{ F g}^{-1}$ , high specific energy density of  $56.4 \text{ Wh kg}^{-1}$ , and flexibility, enabling a practical supercapacitor with a lifespan of 2000 cycles of a desirable retention value.

The fabrication technique for the superaligned ECNFs is based on a facile electrospinning method with a self-designed sample collector; see the schematic diagram in Figure 1a. Different from a normal cylinder design, four steel poles were welded on a plate in order to collect the ECNFs without any substrates. A 10 wt% polyacrylonitrile (PAN,  $M_w = 150\,000$ ) solution in dimethylformamide was electrospun onto the collector. The applied positive voltage was 18 kV and the distance between the needle tip and the collector was 15 cm. The collector was maintained at a rate of 2000 revolutions per minute during the electrospinning to form superaligned precursors. The obtained sheets were then put into a furnace for stabilization to ensure that the fibers did not melt during pyrolysis. The heating rate was  $1 \text{ }^\circ\text{C min}^{-1}$  from room temperature to  $280 \text{ }^\circ\text{C}$  and kept for 6 h. The as-stabilized nanofibers were finally carbonized at

1200 °C for 1 h at a heating rate of 5 °C min<sup>-1</sup> under N<sub>2</sub> atmosphere to yield high mechanical strength ECNFs.

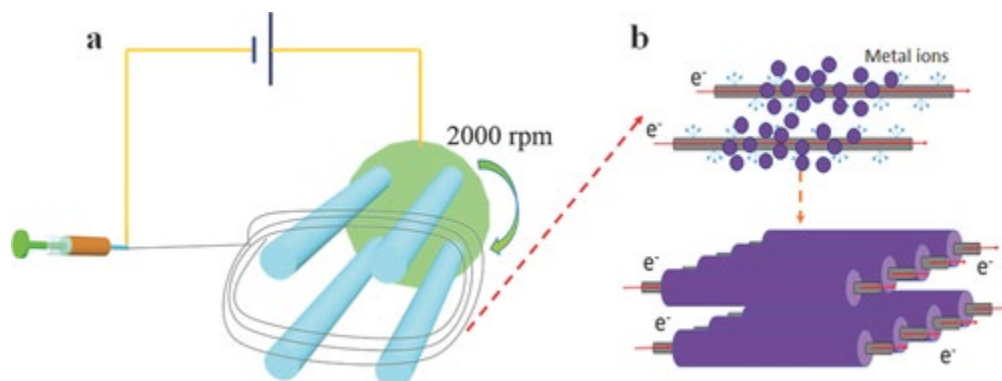


**Figure 1.** a) Illustrations of the aligned electrospinning technique and b) ordered electron flows that initiate uniform electrodeposition on the superaligned ECNFs using a three-electrode setup with an ECNFs working electrode, an Ag/AgCl reference electrode, and a platinum counter electrode.

The as-prepared pure ECNFs exhibit superaligned structure (Figure 2a,b). It is hypothesized that the alignment of ECNFs can reduce disordered electron flow, leading to a more uniform electrodeposition process. A nitric acid pretreatment, which introduces hydroxyl and carboxyl groups, was used to make the ECNFs surface more hydrophilic and to introduce reaction sites for nucleation of MnO<sub>2</sub> crystallites. MnO<sub>2</sub> was electrodeposited onto the ECNFs with a three-electrode setup (Figure 1b). A constant low current (40 μA) was applied by an electrochemical workstation for various times ranging from 0.5 to 4 h under an inert N<sub>2</sub> atmosphere with an aqueous precursor solution containing 10 × 10<sup>-3</sup> m MnSO<sub>4</sub> and 100 × 10<sup>-3</sup> m Na<sub>2</sub>SO<sub>4</sub>. The composites' structure and morphology were characterized by scanning electron microscopy (SEM) (Figure 2c–j). When the electrodeposition starts, small clusters form on the functionalized sites distributed on the fibers (Figure 2c,d). As the electrodeposition continues, the clusters begin to grow larger into a morphology (Figure 2e,f) that is denser than that of the porous flowers reported elsewhere using high current or cyclic voltammetry (CV) techniques in the electrodeposition.<sup>16-18, 32</sup> After electrodeposition for 2 h, the clusters begin to merge with one another to form small balls around the ECNFs; the SEM images clearly show surface structures corresponding to these firmly merged balls (Figure 2g,h). As the electrodeposition time increases, the “kebab”-like structures keep growing until the fibers are fully covered (Figure 2i,j).

A size distribution analysis shows a monotonic increase in average size of the nodules (“kebab”-like structures) with the increase of the electrodeposition time (Figure 2c–j). After electrodeposition for 4 h, the ECNFs with nanofiber diameter of about 208 nm are decorated by an MnO<sub>2</sub> film with a thickness of about 1660 nm, making a total diameter of ≈1868 nm (Figure 2j; Figure S1, Supporting Information). MnO<sub>2</sub> electrodeposition beyond a 4 h time (Figure S2, Supporting Information of 8 h deposition) does not show an obvious increase in thickness with the applied current, a feature that probably arises from the high resistance of the MnO<sub>2</sub> layers. In a control experiment, MnO<sub>2</sub> was electrodeposited on randomly distributed ECNFs using the same electrochemical conditions (Figure S3, Supporting Information). Under

these conditions MnO<sub>2</sub> favors the nucleation and growth of clusters at the junctions of ECNFs rather than the uniform distribution along the fiber surfaces that is found for superaligned ECNFs. These data corroborate the inference that the ECNFs' alignment promotes the homogenous electron flow and facilitates the uniform MnO<sub>2</sub> growth.

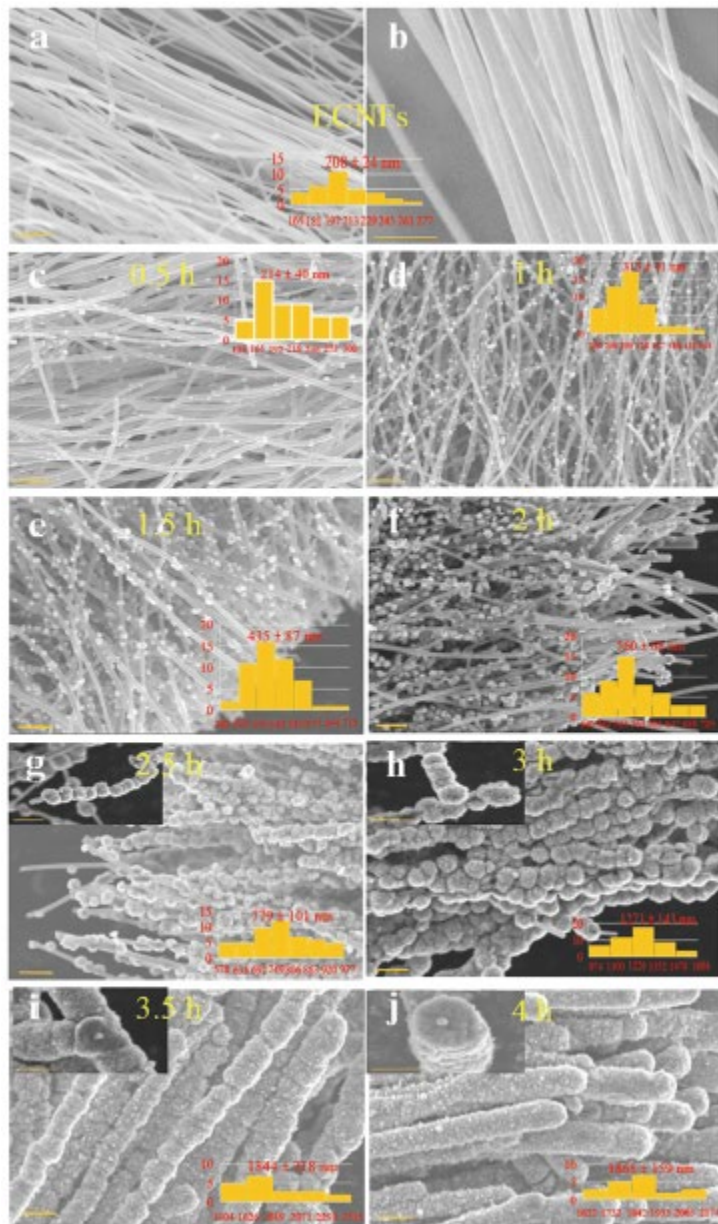


**Figure 2.** SEM images of superaligned ECNFs and MnO<sub>2</sub>/ECNFs for different electrodeposition times from 0.5 to 4 h with the histograms of size distribution analysis. All of the scale bars are 2  $\mu$ m. Note that enlarged images are shown for superaligned ECNFs and MnO<sub>2</sub>/ECNFs (2.5, 3, 3.5, and 4 h).

The chemical composition of the MnO<sub>2</sub>/ECNFs was analyzed by energy dispersive X-ray (EDX) spectroscopy and X-ray photoelectron spectroscopy (XPS). The EDX spectrum (Figure 3a, Figure S4, Supporting Information) shows that the surface composition of the electrochemically

deposited electrodes is composed of the elements C, O, and Mn. The atomic ratio of O and Mn is close to 2:1, which implies the formation of  $\text{MnO}_2$ . The chemical composition of the  $\text{MnO}_2/\text{ECNFs}$  sample was also investigated by XPS. The strong C (supported by ECNFs; Figure S5, Supporting Information), Mn, and O signals in the survey XPS spectrum reveal the existence of Mn atoms (Figure 3b). The high resolution Mn 2p spectra for  $\text{MnO}_2/\text{ECNFs}$  is presented in Figure S6 in the Supporting Information. Two strong peaks at 642.3 and 653.9 eV can be clearly seen, corresponding to the Mn 2p<sub>3/2</sub> and Mn 2p<sub>1/2</sub> spin-orbit peaks of  $\text{MnO}_2$ , respectively.<sup>33, 34</sup> The pronounced peak in the O 1s XPS spectrum (Figure S7, Supporting Information) at 530.0 eV is assigned to Mn–O–Mn in the composite, and the peak at 531.4 eV can be assigned to Mn–OH formation.<sup>35, 36</sup>

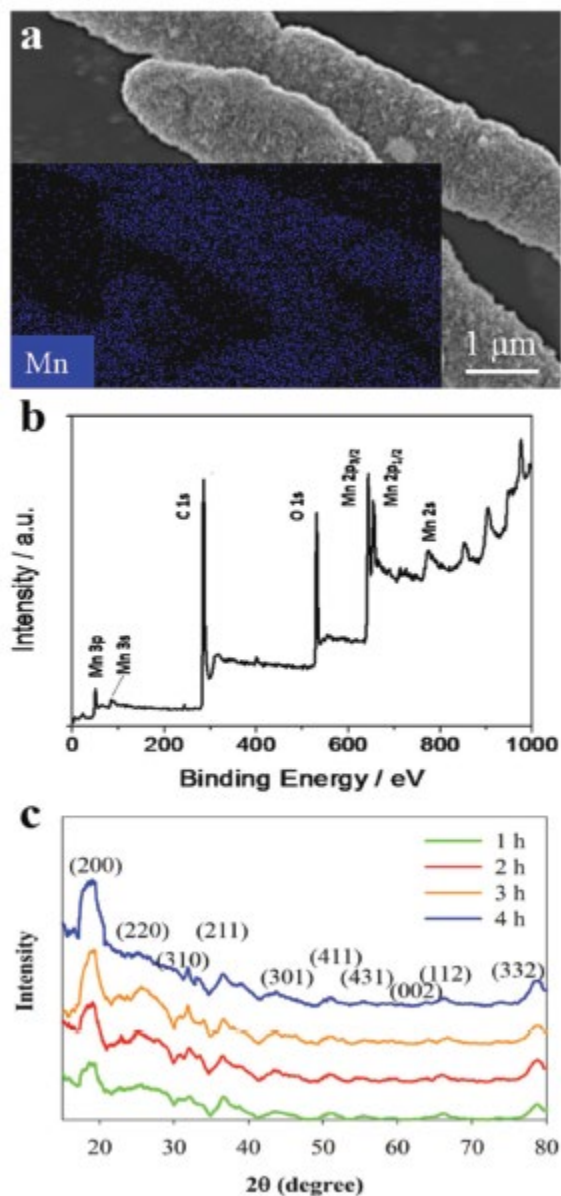


**Figure 3.** a) SEM associated with EDX mapping analysis of the  $\text{MnO}_2/\text{ECNFs}$  under electrodeposition for 4 h. b) XPS spectrum of the  $\text{MnO}_2/\text{ECNFs}$  under electrodeposition for 4 h. c) XRD analysis of the  $\text{MnO}_2/\text{ECNFs}$  under electrodeposition for 1, 2, 3, and 4 h.

To investigate the MnO<sub>2</sub> crystal structure, the as-prepared MnO<sub>2</sub>/ECNFs materials were examined by X-ray diffraction (XRD) (Figure 3c). The XRD patterns could be fully indexed to  $\alpha$ -MnO<sub>2</sub> (JCPDS No. 44-0141), and become more distinct (like the (200) plane) with longer electrodeposition time.<sup>37</sup>

The comprehensive electrodeposition of MnO<sub>2</sub> originates from the stable structure of ECNFs, which contributes to a uniform Mn<sup>2+</sup> flux (Figure 4a). The electrochemical reaction occurs according to<sup>38</sup>

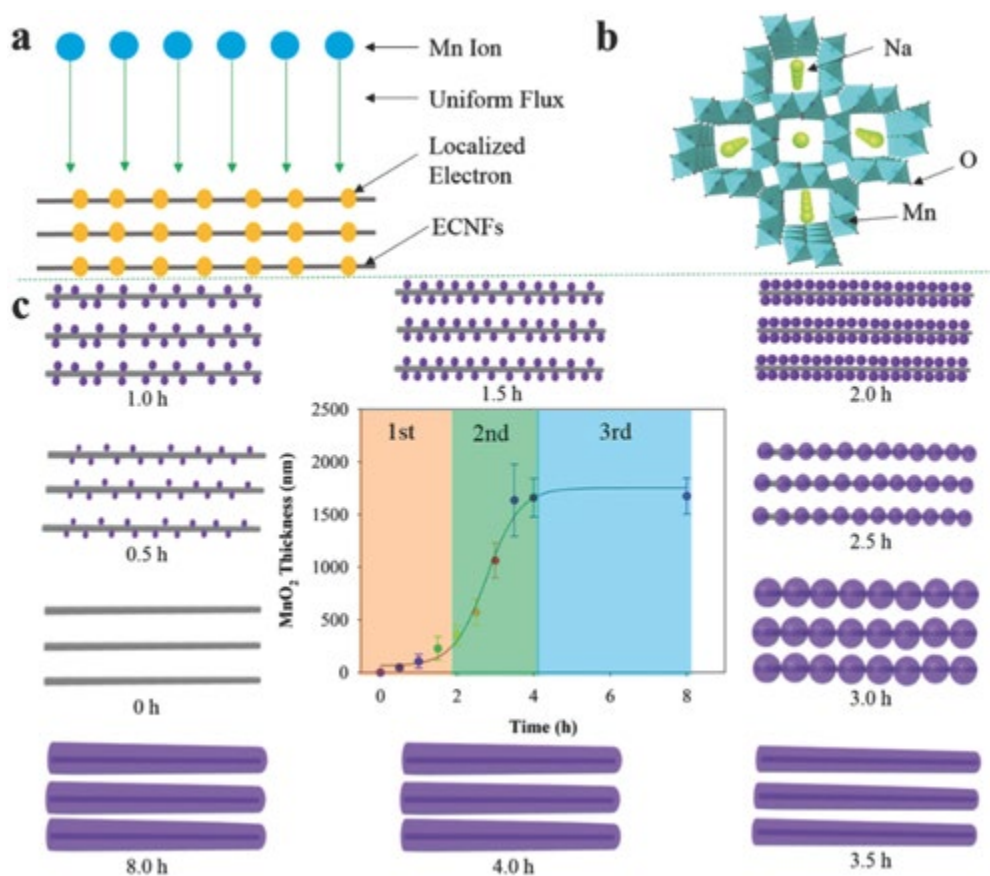
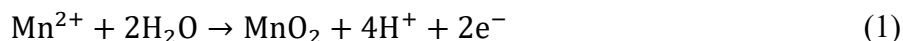


**Figure 4.** Mechanistic view of the MnO<sub>2</sub> growth including the schematic description of a) Mn<sup>2+</sup> uniform flux, b)  $\alpha$ -MnO<sub>2</sub> crystalline , and c) time-dependent MnO<sub>2</sub> growth with data analysis.

The MnO<sub>2</sub> matrix has different structural motifs arising from edge- or corner-sharing MnO<sub>6</sub> octahedra in different connectivity schemes, resulting in channels that extend in a direction parallel to the unit cell; and the MnO<sub>2</sub> appears in a number of crystallographic polymorphs, such as  $\alpha$ -,  $\beta$ -,  $\gamma$ -,  $\delta$ -, and  $\epsilon$ -MnO<sub>2</sub>.<sup>39, 40</sup> In this study, cations (Na<sup>+</sup>) were introduced during the synthetic process, but the 1 × 1 channels (with a size of 0.189 nm) are too small for Na<sup>+</sup> to intercalate and stabilize the structure, which results in the formation of  $\alpha$ -MnO<sub>2</sub>. In contrast double chains of edge-sharing MnO<sub>6</sub> octahedra, which are linked at the corners to form 2 × 2

channels (with a size of 0.46 nm) and  $1 \times 1$  tunnel structures, are large enough for cation placement (Figure 4b).<sup>39, 40</sup> The cations, which reside inside the  $2 \times 2$  channels of  $\alpha$ -MnO<sub>2</sub>, increase the electronic conductivity of the MnO<sub>2</sub>/ECNFs' system and indirectly enhance the electrodeposition of  $\alpha$ -MnO<sub>2</sub>.<sup>41</sup> The time-dependent growth analysis suggests a three-step kinetics mechanism for the electrodeposition (Figure 4c). The first step involves small cluster formation on a boundary layer distributed along the fibers (0–2 h). The second step involves “kebab”-like structure formation and growth from small to big nodules of MnO<sub>2</sub> around the ECNFs (2–4 h). The final step involves the cessation of MnO<sub>2</sub> nodule growth and establishment of a dense film with a self-limiting thickness (>4 h).

In the growth process, the thickness of the MnO<sub>2</sub> film can be controlled by the electrodeposition time (Figure 2). We can write a kinetic equation to describe the MnO<sub>2</sub> growth for the electrodeposition as<sup>42</sup>

$$dh/dt = c(j - j_d) \quad (2)$$

where  $dh/dt$  is the rate of MnO<sub>2</sub> film formation and growth,  $c$  is the coulombic efficiency ( $\text{cm}^3 \text{C}^{-1}$ ),  $j$  is the measured current density, and  $j_d$  is the required current density to prevent dissolution. The measured current density has a nonlinear exponential relationship with the applied voltage ( $V$ )<sup>43</sup>

$$j = A \exp(B \cdot V/h) \quad (3)$$

where  $A$  and  $B$  are characteristic constants of the system. According to the nonlinear relationship between current density and electric field strength, the saturation of film growth is thus given by the equation

$$h_{\max} = BV/(\ln(j_d/A)) \quad (4)$$

Figure 4c shows a best fit of the MnO<sub>2</sub> thickness ( $h$ ) versus deposition time ( $t$ ) data by the equation

$$h = h_{\max}/1 + 10^{(\tau_{0.5}-t)} \quad (t > 0) \quad (5)$$

where  $h_{\max}$  is about 1693 nm and a half-life time constant ( $\tau_{0.5}$ ) is about 2.78 h. The MnO<sub>2</sub> thickness increases in a time-dependent manner (from 0.5 to 8 h) until the MnO<sub>2</sub> thickness is observed to plateau after 4 h of electrodeposition, which supports a three-stage kinetic mechanism for the MnO<sub>2</sub> electrodeposition process.

The as-prepared MnO<sub>2</sub>/ECNFs films were examined for their performance as supercapacitor electrodes. CV studies (Figure 5a; Figure S8, Supporting Information) in a three electrode-electrochemical cell with 6.0 m KOH electrolyte solution were performed to calculate the specific capacitance of the MnO<sub>2</sub>/ECNFs electrodes (details are provided in the Supporting Information). The specific capacitance calculated with respect to the whole mass of the MnO<sub>2</sub>/ECNFs electrodes shows a monotonic increase with the MnO<sub>2</sub> electrodeposition time (up to 4 h). The capacitance of the MnO<sub>2</sub>/ECNFs with 1, 2, 3, and 4 h deposition is 146, 219, 336,

and  $630 \text{ F g}^{-1}$ , respectively.  $\text{MnO}_2/\text{ECNF}$  electrodes with less than 2 h electrodeposition time show an enhanced specific capacitance as compared to bare ECNFs (Figure S9, Supporting Information) while maintaining flat (parallelogram) voltammogram shapes. Moreover, the  $\text{MnO}_2/\text{ECNF}$ s electrode possesses a combined contribution of the electrochemical double layer capacitance and the pseudocapacitance from  $\text{MnO}_2$ . The double layer stores charge electrostatically, mainly based on the specific surface area and the adsorption of ions at electrode surface. The pseudo-capacitance depends on the reversible redox reactions between  $\text{Mn(IV)/Mn(III)}$  species and  $\text{K}^+$  intercalation/deintercalation at the  $\text{MnO}_2/\text{electrolyte}$  interfaces.<sup>44-46</sup> The longer electrodeposition (3 and 4 h) results in thicker and more uniform  $\text{MnO}_2$  films, which enhances the successive multiple surface redox reactions between the  $\text{Mn(IV)/Mn(III)}$  complexes as the redox peaks in Figure 5a shown.

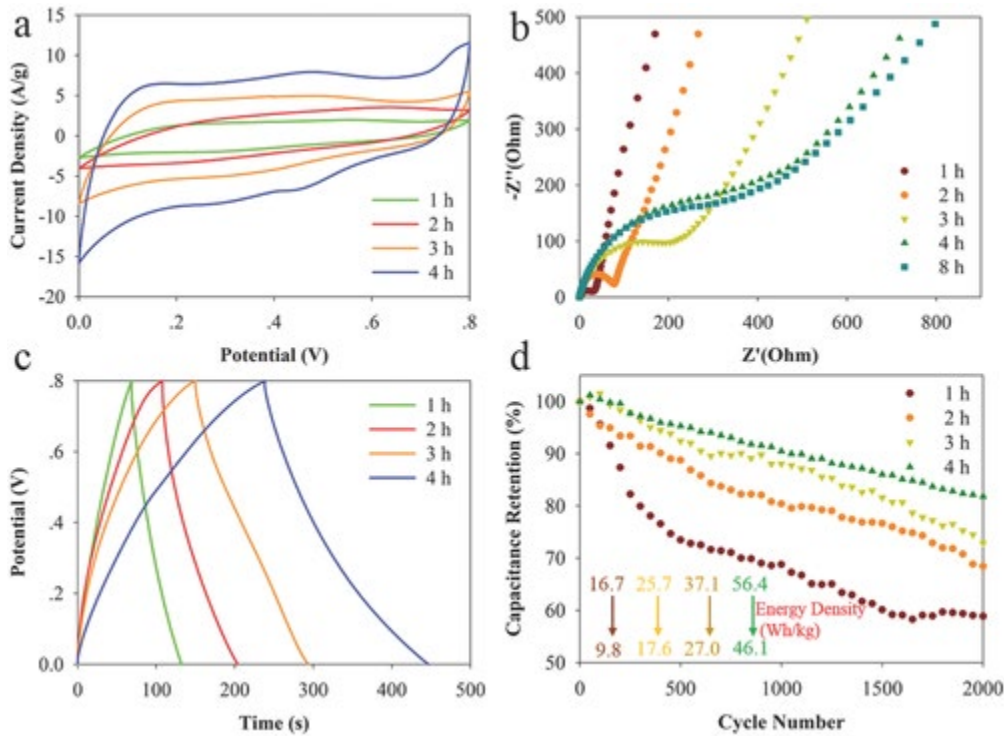


**Figure 5.** Electrochemical characterization of the films includes a) cyclic voltammetry at  $20 \text{ mV s}^{-1}$  in  $6.0 \text{ m KOH}$  electrolyte solution, b) electrochemical impedance spectroscopy at frequencies from  $100 \text{ kHz}$  to  $0.1 \text{ Hz}$ , c) galvanic charge–discharge profiles at  $1 \text{ A g}^{-1}$ , and d) retention performance of  $\text{MnO}_2/\text{ECNF}$ s under 1, 2, 3, and 4 h electrodeposition. Note that the impedance spectra also include an 8 h electrodeposition data and the insert in (d) shows the specific energy density changes after 2000 cycles.

The electrochemical equilibrium involves the  $\text{KOH}$  electrolyte and can be expressed as<sup>7,47</sup>



In addition, the presence of  $\text{K}^+$  inside the  $2 \times 2$  channels of the  $\alpha\text{-MnO}_2$  has a strong beneficial effect on the electrochemical performance of the electrodes by enhancing the electronic conductivity through electron hopping between  $\text{Mn}^{4+}/\text{Mn}^{3+}$ . The  $\text{MnO}_2/\text{ECNF}$ s electrodes with 3

h (charge transfer resistance of about 257 Ohms) and 4 h (charge transfer resistance of about 326 Ohms) electrodeposition have higher resistance, which is deduced from the electrochemical impedance spectroscopy (EIS) Nyquist plots (Figure 5b) and a Randles circuit model (Figure S10, Supporting Information). These plots consist of a semicircle in the high-frequency region and a straight line in the low-frequency region, which display an increase in charge transfer resistance and diffusive resistance with an increase in electrodeposition time.<sup>48, 49</sup> No obvious difference was found between the 4 and 8 h electrodeposited MnO<sub>2</sub>/ECNFs, further corroborating the conclusion that MnO<sub>2</sub> film growth ceases after 4 h of electrodeposition.

The galvanic charge/discharge time under longer electrodeposition time increases more significantly than that under shorter electrodeposition time (Figure 5c; Figure S11, Supporting Information). Note that both EIS and galvanic charge–discharge were tested in a self-designed symmetrical capacitor platform (Figure S12, Supporting Information) assembled in a glove box. For practical purposes, retention tests were also performed for up to 2000 cycles of charge and discharge at current densities of 1 A g<sup>-1</sup>. Figure 5d shows the first cycle of each sample and its specific energy density is 16.7, 25.7, 37.1, and 56.4 Wh kg<sup>-1</sup>, respectively. Considering that a power density of around 1 kW kg<sup>-1</sup> was achieved at the current density of 10 A g<sup>-1</sup>, it is superior among most recent reports (Figure S13,<sup>50-53</sup> Supporting Information). After 2000 cycles, the MnO<sub>2</sub>/ECNFs electrode with 1 h electrodeposition drops to 58.9% of its initial energy density. This loss may occur because the small MnO<sub>2</sub> clusters have higher surface contact with the electrolyte and undergo irreversible solvation and reduction. The MnO<sub>2</sub>/ECNFs electrodes with 2 and 3 h electrodeposition show higher retention performances of 68.4% and 72.9%, respectively. The 4 h MnO<sub>2</sub>/ECNFs electrode has the highest retention value of 81.8% (an extended test of 5000 cycles were performed with retention value of 66.7% in Figure S14, Supporting Information) which agrees with the conclusion that the compact and uniform MnO<sub>2</sub> coatings provide stable ion exchange and charge–discharge rates while maintaining a high pseudocapacitance. In order to verify its flexibility, a folding test was also performed. The 4 h MnO<sub>2</sub>/ECNFs electrode can be folded at different degrees within 2% changes in discharge time. (Figure S15, Supporting Information)

This work demonstrates a new strategy for uniformly electrodepositing MnO<sub>2</sub> on aligned ECNFs and the change in the mechanism of MnO<sub>2</sub> growth with the electrodeposition time was explored. In contrast to earlier studies with a much higher current, the reported electrodeposition was conducted with a constant low current of 40 μA. Film growth proceeds by a three-stage kinetic process with a halfway growth time of 2.78 h. From the electrochemical performance, MnO<sub>2</sub>/ECNFs with a 4 h electrodeposition display a high capacitance of 630 F g<sup>-1</sup> and a specific energy density of 56.4 Wh kg<sup>-1</sup>. These findings represent a significant improvement in stable metal oxide/carbonaceous nanomaterial-based pseudocapacitance energy storage.

## Experimental Section

*MnO<sub>2</sub> Electrodeposition on ECNFs:* After the superaligned ECNFs were prepared, MnO<sub>2</sub> was electrodeposited onto 1 cm<sup>2</sup> ECNFs by a galvanostatic method with a three-electrode setup using a charging current of 40 μA. Here, an Au electrode taped with ECNFs, platinum wire, and Ag/AgCl were used as working electrode, counter electrode, and reference electrode, respectively. To assure that the deposition of MnO<sub>2</sub> took place uniformly and firmly at the

ECNFs' surfaces, the ECNFs electrode was treated with 4 M HNO<sub>3</sub> solution at 70 °C for 2 h to introduce –OH and –COOH groups to facilitate the deposition. An aqueous precursor solution with 10 × 10<sup>-3</sup> m MnSO<sub>4</sub> and 100 × 10<sup>-3</sup> m Na<sub>2</sub>SO<sub>4</sub> was used as the supporting electrolyte. After the deposition, the working electrodes were washed with deionized water and then dried at 80 °C for 5 h. The mass was weighed before and after deposition, and mass loading of MnO<sub>2</sub> on ECNFs at different deposition time from 0.5 to 4 h is shown in Table S1 in the Supporting Information.

*Materials Characterization:* Field emission scanning electron microscope (FESEM) (Carl Zeiss Auriga-BU FIB FESEM Microscope) was performed to study the morphological properties of MnO<sub>2</sub>/ECNFs. X-ray powder diffraction (XRD) (Agilent Technologies Oxford Germini X-Ray Diffractometer) was employed to study the crystal structures of MnO<sub>2</sub>/ECNFs. EDX spectroscopy (Hitachi S-4800-I FESEM w/Backscattered Detector & EDX) was performed to study the atomic ratio on MnO<sub>2</sub>/ECNFs. XPS (Thermo Fisher ESCALAB 250 Xi) was used to determine the elemental composition of MnO<sub>2</sub>/ECNFs.

*Electrochemical Measurements:* Electrochemical performance of the as-prepared electrodes was performed on a biologic VMP3 electrochemical workstation using a three-electrode system with a platinum wire as the counter-electrode and Ag/AgCl as the reference electrode in a 6 m KOH electrolyte solution. The ECNFs film was cut into 1 cm<sup>2</sup> pieces for CV, EIS, and galvanostatic charge/discharge experiments. The voltammetry was scanned from a potential of 0.0 to 0.8 V versus Ag/AgCl at different scan rates. EIS was performed from 100 kHz to 0.1 Hz, and charge/discharge tests were performed at different current densities.

### Acknowledgements

Y.L. and Z.Z. contributed equally to this work. J.W., Y.L., and Z.Z. acknowledge the NC State funding through Joint School of Nanoscience and Nanoengineering (JSNN). B.B. and D.H.W. acknowledge support from DOE Grant ER46430. The authors would like to thank Dr. Lifeng Zhang at North Carolina A&T State University for helping on ECNFs fabrication. This work was performed at the JSNN, a member of Southeastern Nanotechnology Infrastructure Corridor (SENIC) and National Nanotechnology Coordinated Infrastructure (NNCI), which is supported by the National Science Foundation (ECCS-1542174).

### Conflict of Interest

The authors declare no conflict of interest.

### References

1. S. Mann, *Angew. Chem., Int. Ed.* 2000, **39**, 3392.
2. M. Antonietti, G. A. Ozin, *Chem. Eur. J.* 2004, **10**, 28.
3. H. Cölfen, S. Mann, *Angew. Chem., Int. Ed.* 2003, **42**, 2350.
4. P. Poizot, S. Laruelle, S. Grugeon, L. Dupont, J. M. Tarascon, *Nature* 2000, **407**, 496.
5. J. M. Tarascon, M. Armand, *Nature* 2001, **414**, 359.
6. N. Fukata, M. Mitome, Y. Bando, W. Wu, Z. L. Wang, *Nano Energy* 2016, **26**, 37.
7. P. Simon, Y. Gogotsi, *Nat. Mater.* 2008, **7**, 845.
8. L. L. Zhang, X. S. Zhao, *Chem. Soc. Rev.* 2009, **38**, 2520.

9. X. Xia, J. Tu, Y. Zhang, J. Chen, X. Wang, C. Gu, C. Guan, J. Luo, H. J. Fan, *Chem. Mater.* 2012, **24**, 3793.
10. R. Liu, S. B. Lee, *J. Am. Chem. Soc.* 2008, **130**, 2942.
11. M. Antonietti, G. A. Ozin, *Chem. Eur. J.* 2004, **10**, 28.
12. H. Cölfen, S. Mann, *Angew. Chem., Int. Ed.* 2003, **42**, 2350.
13. Y. Wu, T. Zhang, F. Zhang, Y. Wang, Y. Ma, Y. Huang, Y. Liu, Y. Chen, *Nano Energy* 2012, **1**, 820.
14. S. Arico, P. Bruce, B. Scrosati, J.-M. Tarascon, W. van Schalkwijk, *Nat Mater* 2005, **4**, 366.
15. L. Hu, W. Chen, X. Xie, N. Liu, Y. Yang, H. Wu, Y. Yao, M. Pasta, H. N. Alshareef, Y. Cui, *Acs Nano* 2011, **5**, 8904.
16. Y. Jiang, X. Ling, Z. Jiao, L. Li, Q. Ma, M. Wu, Y. Chu, B. Zhao, *Electrochim. Acta* 2015, **153**, 246.
17. P. Yang, Y. Chen, X. Yu, P. Qiang, K. Wang, X. Cai, S. Tan, P. Liu, J. Song, W. Mai, *Nano Energy* 2014, **10**, 108.
18. C. Choi, S. H. Kim, H. J. Sim, J. A. Lee, A. Y. Choi, Y. T. Kim, X. Lepró, G. M. Spinks, R. H. Baughman, S. J. Kim, *Sci. Rep.* 2015, **5**, 9387.
19. K. Liang, T. Gu, Z. Cao, X. Tang, W. Hu, B. Wei, *Nano Energy* 2014, **9**, 245.
20. R. Amade, E. Jover, B. Caglar, T. Mutlu, E. Bertran, *J. Power Sources* 2011, **196**, 5779.
21. L. Peng, X. Peng, B. Liu, C. Wu, Y. Xie, G. Yu, *Nano Lett.* 2013, **13**, 2151.
22. S.-M. Li, Y.-S. Wang, S.-Y. Yang, C.-H. Liu, K.-H. Chang, H.-W. Tien, N.-T. Wen, C.-C. M. Ma, C.-C. Hu, *J. Power Sources* 2013, **225**, 347.
23. L. Deng, Z. Hao, J. Wang, G. Zhu, L. Kang, Z.-H. Liu, Z. Yang, Z. Wang, *Electrochim. Acta* 2013, **89**, 191.
24. D. Momodu, A. Bello, J. Dangbegnon, F. Barzegeer, F. Taghizadeh, M. Fabiane, A. T. C. Johnson, N. Manyala, *AIP Adv.* 2014, **4**, 097122.
25. Y. He, W. Chen, J. Zhou, X. Li, P. Tang, Z. Zhang, J. Fu, E. Xie, *ACS Appl. Mater. Interfaces* 2014, **6**, 210.
26. Z. Yu, M. McInnis, J. Calderon, S. Seal, L. Zhai, J. Thomas, *Nano Energy* 2015, **11**, 611.
27. J.-G. Wang, Y. Yang, Z.-H. Huang, F. Kang, *Carbon* 2013, **61**, 190.
28. Y. Liu, Z. Zeng, J. Wei, *Front. Nanosci. Nanotechnol.* 2016, **2**, 78.
29. H. Zhang, G. Cao, Z. Wang, Y. Yang, Z. Shi, Z. Gu, *Nano Lett.* 2008, **8**, 2664.
30. Z. Zeng, Y. Liu, W. Zhang, H. Chevva, J. Wei, *J. Power Sources* 2017, **358**, 22.
31. Aboagye, H. Elbohy, A. D. Kelkar, Q. Qiao, J. Zai, X. Qian, L. Zhang, *Nano Energy* 2015, **11**, 550.
32. J. Sodtipinta, W. Pon-On, W. Veerasai, S. M. Smith, P. Pakawatpanurut, *Mater. Res. Bull.* 2013, **48**, 1204.
33. S. W. Lee, J. Kim, S. Chen, P. T. Hammond, Y. Shao-Horn, *ACS Nano* 2010, **4**, 3889.
34. W. Zilong, Z. Zhu, J. Qiu, S. Yang, *J. Mater. Chem. C* 2014, **2**, 1331.
35. L. Yuan, X.-H. Lu, X. Xiao, T. Zhai, J. Dai, F. Zhang, B. Hu, X. Wang, L. Gong, J. Chen, C. Hu, Y. Tong, J. Zhou, Z. L. Wang, *ACS Nano* 2012, **6**, 656.
36. J.-G. Wang, Y. Yang, Z.-H. Huang, F. Kang, *J. Mater. Chem.* 2012, **22**, 16943.
37. P. Yu, X. Zhang, D. Wang, L. Wang, Y. Ma, *Cryst. Growth Des.* 2009, **9**, 528.
38. S. Devaraj, N. Munichandraiah, *Electrochem. Solid-State Lett.* 2005, **8**, A373.
39. T. Gao, H. Fjellvåg, P. Norby, *Anal. Chim. Acta* 2009, **648**, 235.
40. W. Xiao, D. Wang, X. W. Lou, *J. Phys. Chem. C* 2010, **114**, 1694.

41. Y. Yuan, C. Zhan, K. He, H. Chen, W. Yao, S. Sharifi-Asl, B. Song, Z. Yang, A. Nie, X. Luo, H. Wang, S. M. Wood, K. Amine, M. S. Islam, J. Lu, R. Shahbazian-Yassar, *Nat. Commun.* 2016, **7**, 13374.
42. K. J. Vetter, in *Electrochemical Kinetics*, (Eds.: S. Bruckenstein, B. Howard), Academic Press, New York 1967, pp. 396–454, Ch. 3.
43. P. E. Pierce, Z. Kovac, C. Higginbotham, *Ind. Eng. Chem. Prod. Res. Dev.* 1978, **17**, 317.
44. S. Chen, J. Zhu, X. Wu, Q. Han, X. Wang, *ACS Nano* 2010, **4**, 2822.
45. Z. Fan, J. Yan, T. Wei, L. Zhi, G. Ning, T. Li, F. Wei, *Adv. Func. Mater.* 2011, **21**, 2366.
46. X. Dong, X. Wang, J. Wang, H. Song, X. Li, L. Wang, M. B. Chan-Park, C. M. Li, P. Chen, *Carbon* 2012, **50**, 4865.
47. M. Toupin, T. Brousse, D. Bélanger, *Chem. Mater.* 2004, **16**, 3184.
48. C. Shang, S. Dong, S. Wang, D. Xiao, P. Han, X. Wang, L. Gu, G. Cui, *ACS Nano* 2013, **7**, 5430.
49. J. Xu, S. Gai, F. He, N. Niu, P. Gao, Y. Chen, P. Yang, *Dalton Trans.* 2014, **43**, 11667.
50. S.-C. Lin, Y.-T. Lu, Y.-A. Chien, J.-A. Wang, T.-H. You, Y.-S. Wang, C.-W. Lin, C.-C. M. Ma, C.-C. Hu, *J. Power Sources* 2017, **362**, 258.
51. Y. Lv, H. Che, A. Liu, J. Mu, C. Dai, X. Zhang, Y. Bai, G. Wang, Z. Zhang, *J. Appl. Electrochem.* 2017, **47**, 433.
52. M. Cakici, R. R. Kakarla, F. Alonso-Marroquin, *Chem. Eng. J.* 2017, **309**, 151.
53. W. Quan, C. Jiang, S. Wang, Y. Li, Z. Zhang, Z. Tang, F. Favier, *Electrochim. Acta* 2017, **247**, 1072.

## Supporting Information

# Stable Low-current Electrodeposition of $\alpha$ -MnO<sub>2</sub> on Super-aligned Electrospun Carbon Nanofibers for High-performance Energy Storage

*Yiyang Liu,<sup>a‡</sup> Zheng Zeng,<sup>a‡</sup> Brian Bloom,<sup>b</sup> David H. Waldeck,<sup>b</sup> Jianjun Wei,<sup>a\*</sup>*

<sup>a</sup>Department of Nanoscience, Joint School of Nanoscience and Nanoengineering, University of North Carolina at Greensboro, Greensboro, NC 27401, USA.

<sup>b</sup>Department of Chemistry, University of Pittsburgh, Pittsburgh, PA, 15260

<sup>#</sup>These authors contributed equally to this work.

\*To whom correspondence should be addressed

## EXPERIMENTAL

**MnO<sub>2</sub> electrodeposition on ECNFs.** After the super-aligned ECNFs were prepared, MnO<sub>2</sub> was electrodeposited onto 1 cm<sup>2</sup> ECNFs by a galvanostatic method with a three-electrode setup using a charging current of 40  $\mu$ A. Here, an Au electrode taped with ECNFs, platinum wire, and Ag/AgCl were used as working electrode, counter electrode, and reference electrode, respectively. To assure that the deposition of MnO<sub>2</sub> took place uniformly and firmly at the ECNFs' surfaces, the ECNFs electrode was treated with 4 M HNO<sub>3</sub> solution at 70 °C for 2 h to introduce –OH and –COOH groups to facilitate the deposition. An aqueous

precursor solution with 10 mM MnSO<sub>4</sub> and 100 mM Na<sub>2</sub>SO<sub>4</sub> was used as the supporting electrolyte. After the deposition, the working electrodes were washed with deionized water and then dried at 80 °C for 5 h.

**Materials characterization.** Field emission scanning electron microscope (FESEM) (Carl Zeiss Auriga-BU FIB FESEM Microscope) was performed to study the morphological properties of MnO<sub>2</sub>/ECNFs. X-ray powder diffraction (XRD) (Agilent Technologies Oxford Gemini X-Ray Diffractometer) was employed to study the crystal structures of MnO<sub>2</sub>/ECNFs. Energy-dispersive X-ray spectroscopy (EDX) (Hitachi S-4800-I FESEM w/Backscattered Detector & EDX) was performed to study the atomic ratio on MnO<sub>2</sub>/ECNFs. X-ray photoelectron spectroscopy (XPS, Thermo Fisher ESCALAB 250 Xi) was used to determine the elemental composition of MnO<sub>2</sub>/ECNFs.

**Electrochemical measurements.** Electrochemical performance of the as-prepared electrodes was performed on a bio-logic VMP3 electrochemical workstation using a three-electrode testing system with a platinum wire as the counter-electrode and Ag/AgCl as the reference electrode in a 6 M KOH electrolyte solution. The ECNFs film was cut into 1 cm<sup>2</sup> pieces for cyclic voltammetry (CV), electrochemical impedance spectroscopy (EIS), and galvanostatic charge/discharge experiments. The voltammetry was scanned from a potential of 0.0 V to 0.8 V vs Ag/AgCl at a scan rate of 20 mV s<sup>-1</sup>. Electrochemical impedance spectroscopy (EIS) was performed from 100 kHz to 0.1 Hz, and charge/discharge tests were performed at a current density of 1 A g<sup>-1</sup>.

## CALCULATION SECTION

### Specific capacitance

From the cyclic voltammograms, the specific capacitance was calculated using the following equation: <sup>1-3</sup>

$$C = \int_{E_1}^{E_2} \frac{idE}{2mS(E_2 - E_1)} \quad (1)$$

From the charge/discharge curves, the specific capacitance was calculated using the following equation:

$$C = \frac{It}{m(E_2 - E_1)} \quad (2)$$

where  $C$  is the specific capacitance (F/g),  $\int_{E_1}^{E_2} idE$  is the integrated area in the voltammograms,  $m$  is the mass of the active sample (g),  $S$  is the scan rate (V/s),  $(E_2 - E_1)$  is the potential window (V),  $I$  is the discharge current (A), and  $t$  is the discharge time in the potential window (s).

### Energy density

The energy density ( $D_e$ ) of the capacitors was calculated using the following equation:

$$D_e = C(E_2 - E_1)^2 / 2 \quad (3)$$

### Power density

The power density ( $D_p$ ) of the capacitors was calculated using the following equation:

$$D_e = D_p / t \quad (4)$$

where  $t$  is the discharge time.

## Supplemental Figures

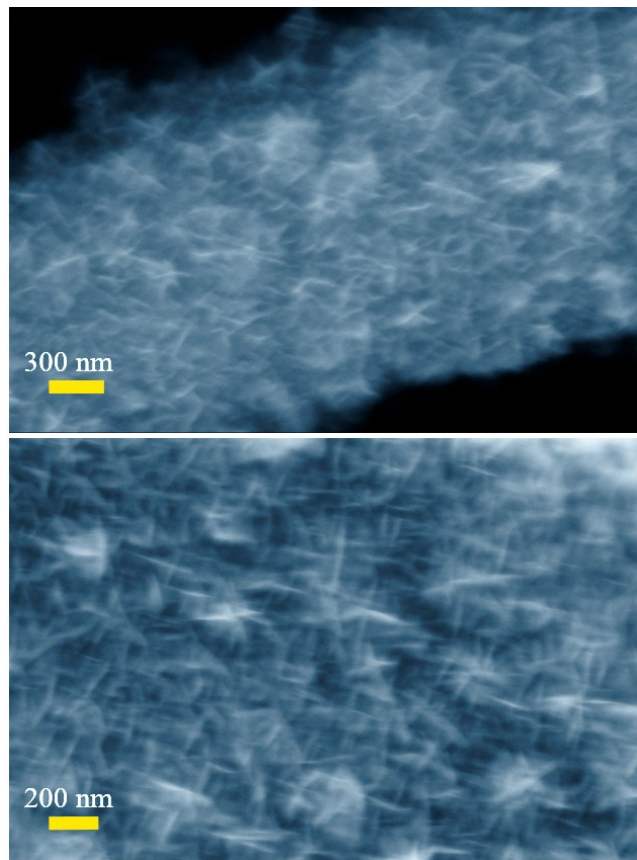


Fig. S1. SEM image of aligned MnO<sub>2</sub>/ECNFs after deposition time for 4 hours.

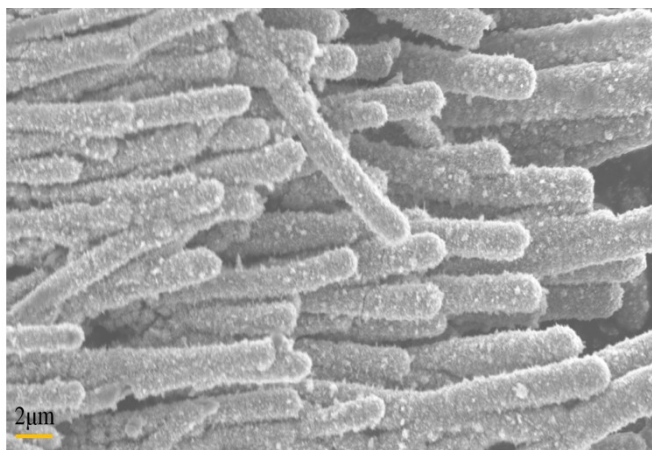


Fig. S2. SEM image of aligned MnO<sub>2</sub>/ECNFs after deposition time for 8 hours.

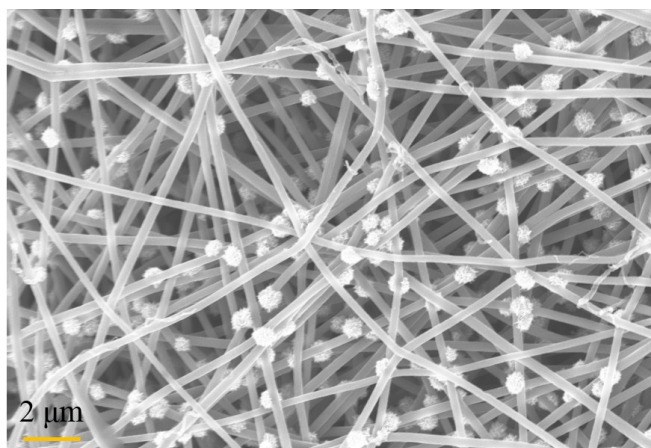


Fig. S3. SEM image of MnO<sub>2</sub>/ECNFs without alignment after deposition time for 3 hours.

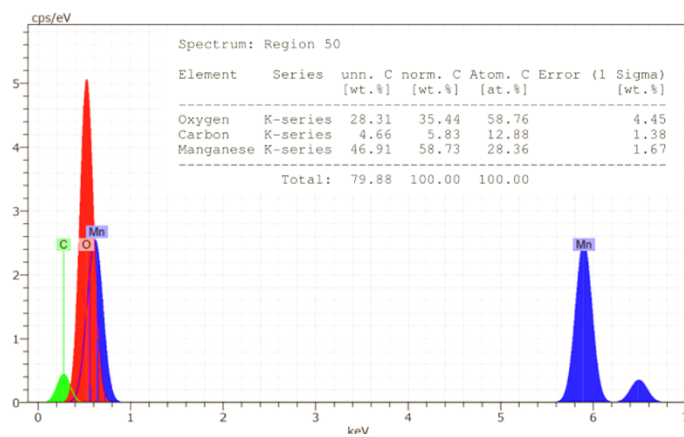


Fig. S4 EDX of MnO<sub>2</sub>/ECNFs after electrodeposition for 4 hours. The atom% of C, O and Mn is 12.88%, 58.76%, 28.36% respectively.

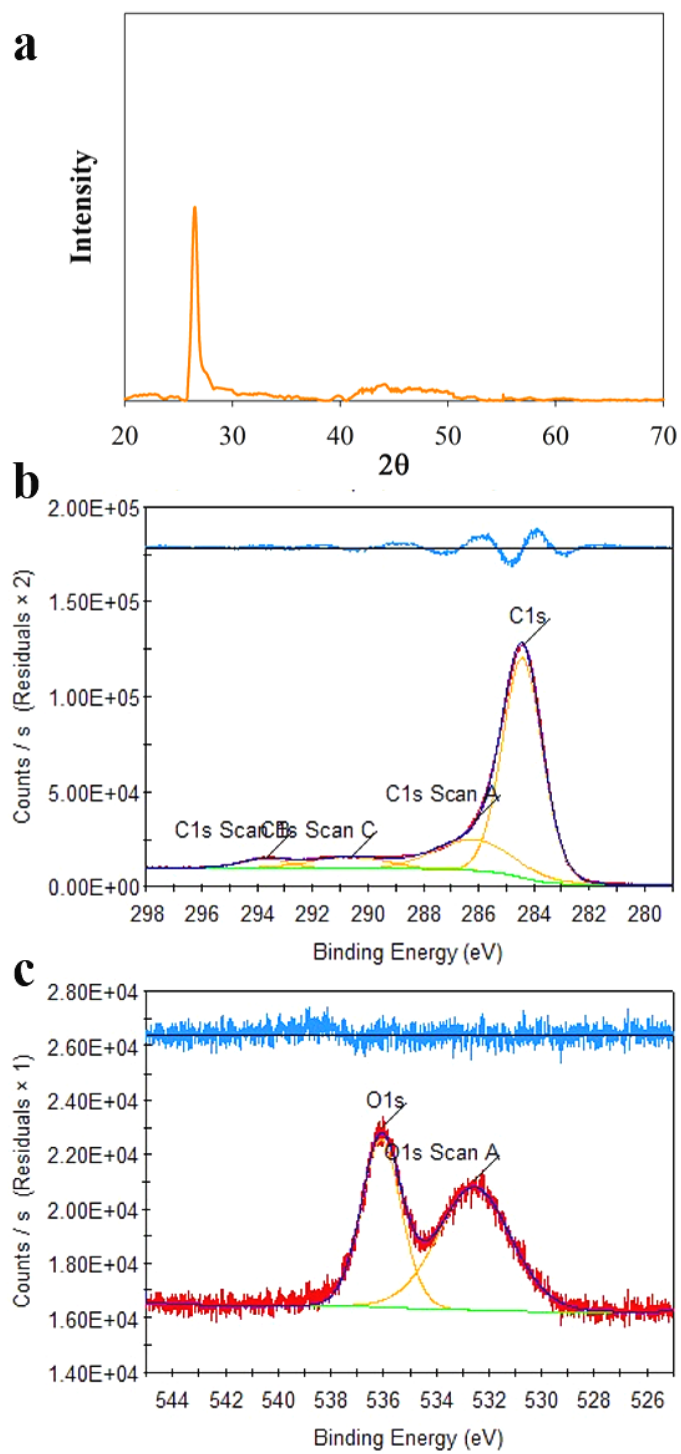


Fig. S5. XRD (a) and XPS (with C (b) and O (c)) of the pure ECNFs.

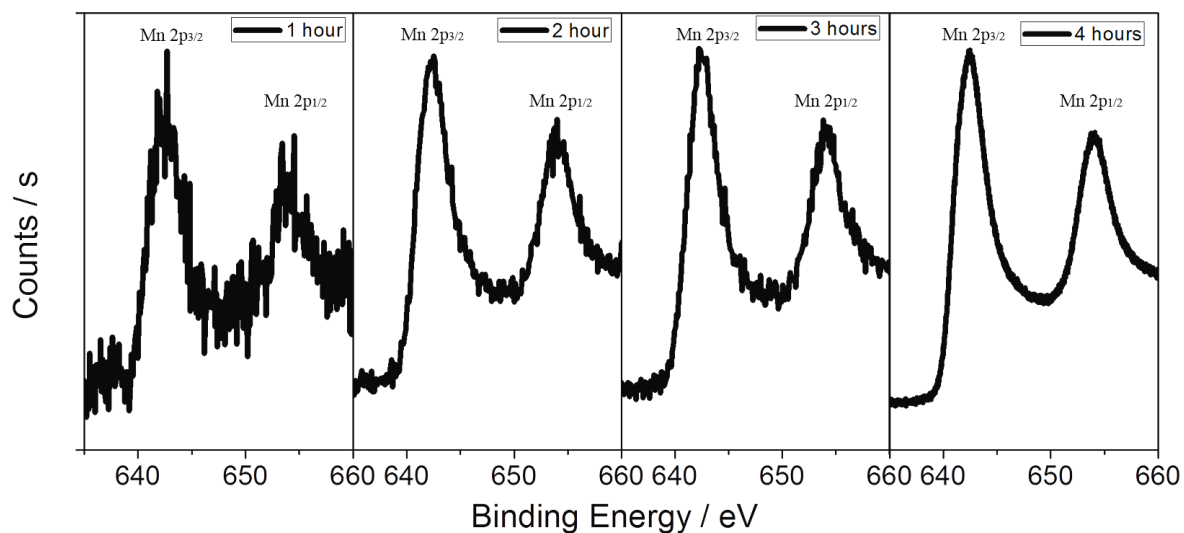


Fig. S6. Mn 2P XPS spectrum of the MnO<sub>2</sub>/ECNFs under electrodeposition for 1 h, 2 h, 3 h, and 4 h.

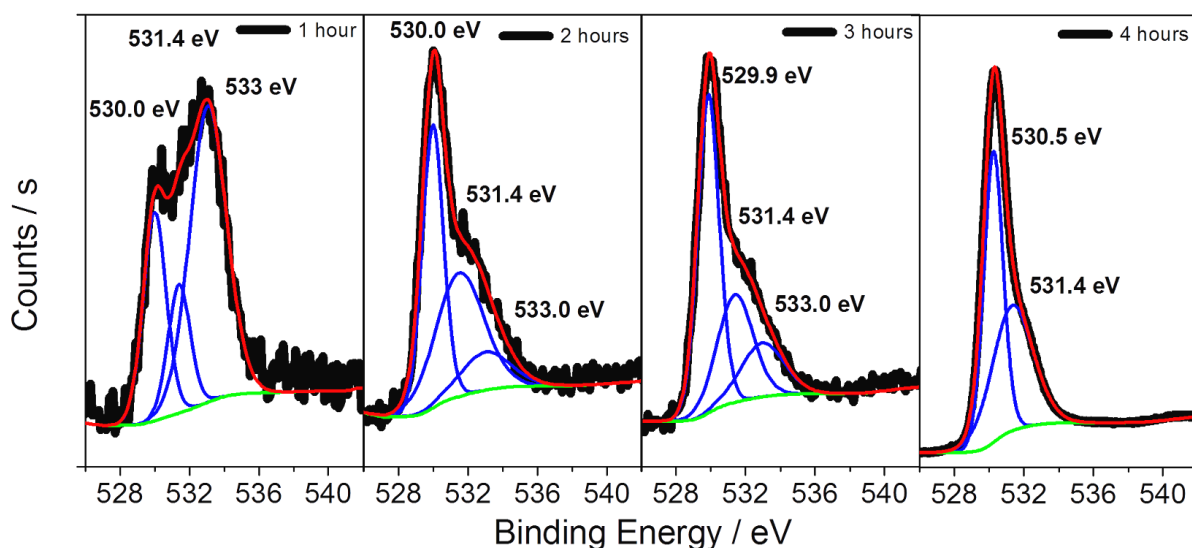


Fig. S7. O 1s XPS spectrum (black line) and its simulated peak fitting (blue lines) of the MnO<sub>2</sub>/ECNFs under electrodeposition for 1 h, 2 h, 3 h, and 4 h. The green line is the background for the XPS spectrum. The peak at 530.0 is associated with Mn-O-Mn, the peak at 531.4 is associated with Mn-OH and the peak at 533.0 is associated with H-O-H.

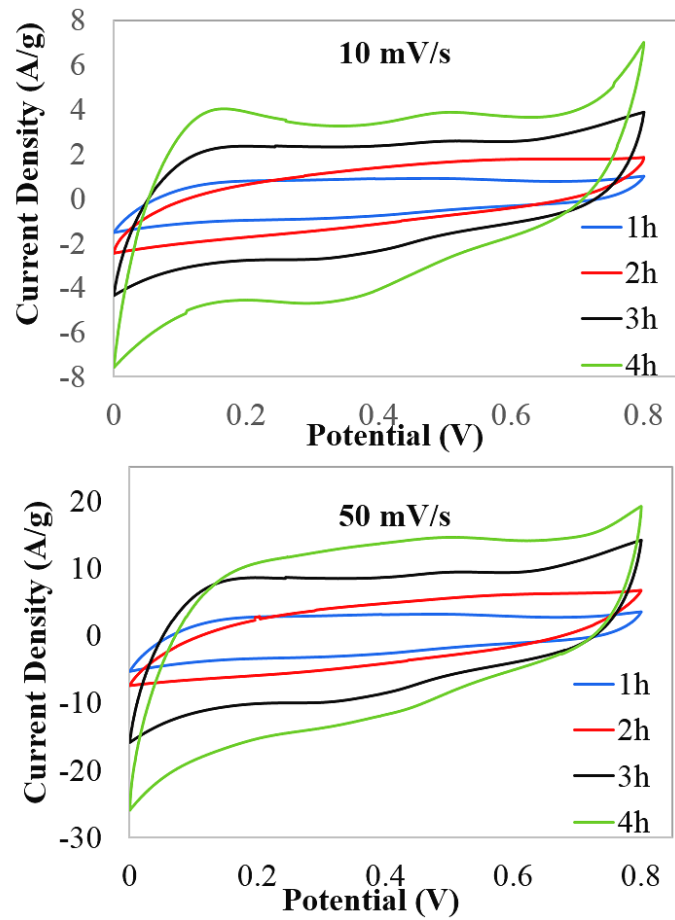


Fig. S8. Cyclic voltammetry of MnO<sub>2</sub>/ECNFs electrodes at 10 mV/s and 50 mV/s in 6.0 M KOH electrolyte solution.

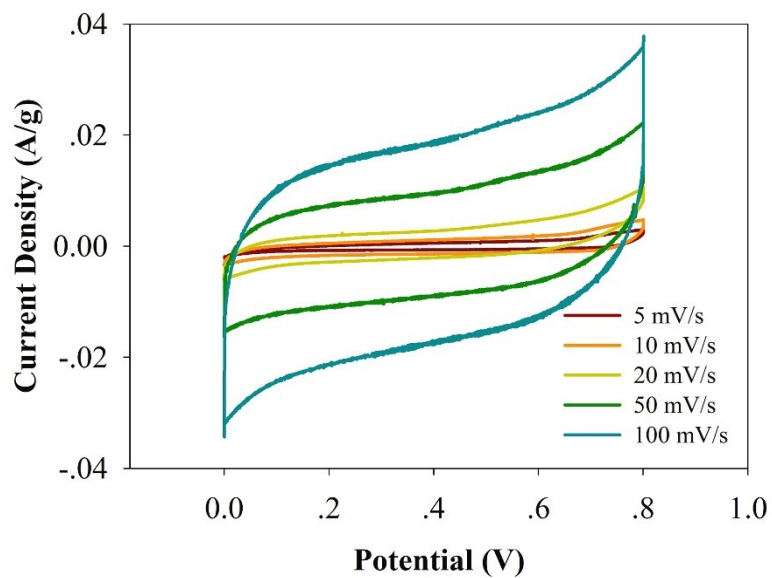


Fig. S9. Cyclic voltammograms of the pure ECNFs electrodes tested at different scan rates.

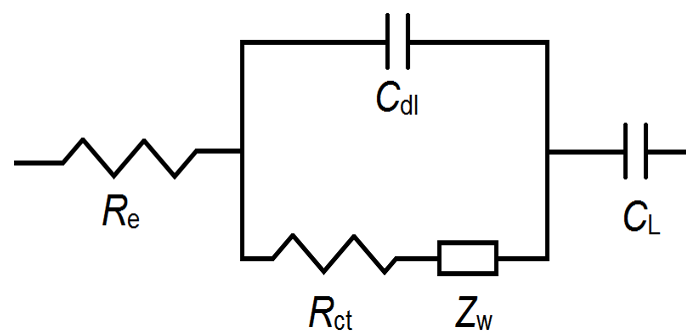


Fig. S10. Schematic of Randles circuit of  $\text{MnO}_2/\text{ECNFs}$  electrodes.

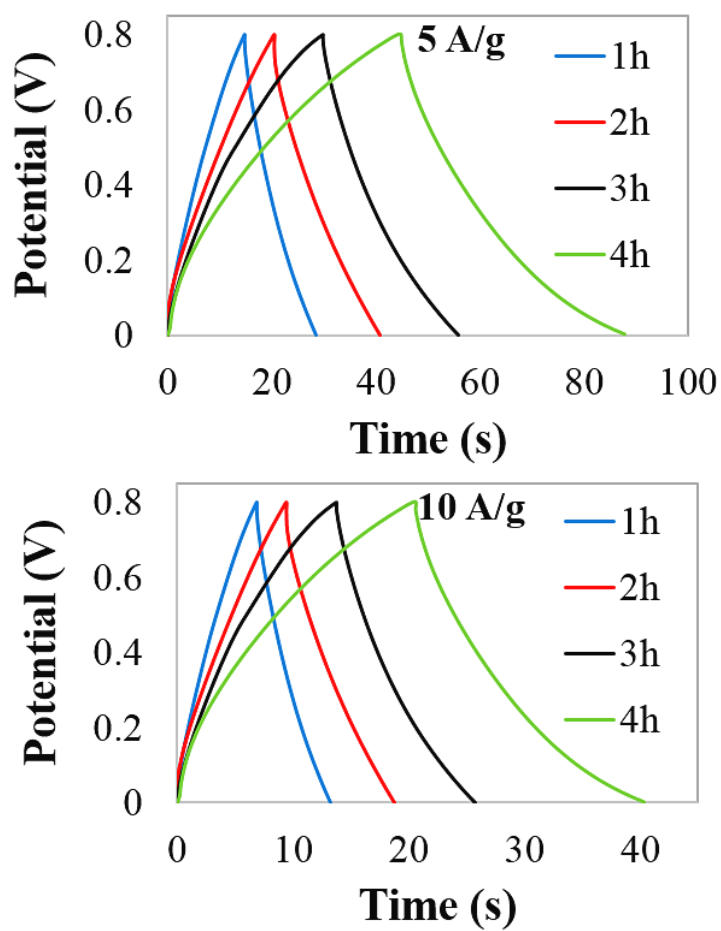


Fig. S11. Galvanic charge-discharge profiles of  $\text{MnO}_2/\text{ECNFs}$  electrodes at 5 A/g and 10 A/g.

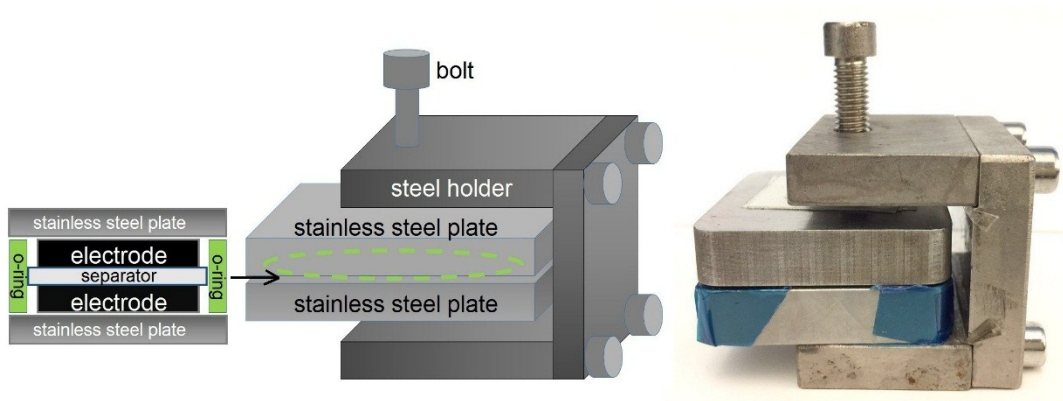


Fig. S12. Schematic and photo of a self-designed platform.

The self-designed platform consisting of two stainless steel plates as current collectors, an o-ring to seal the cell, U-shape holder and a fasten bolt to adjust the distance between the electrodes.

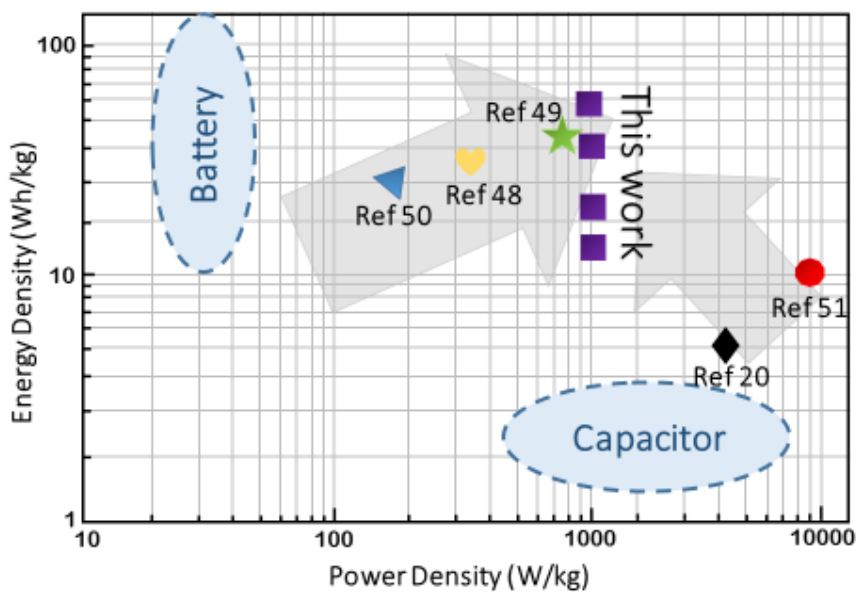


Fig. S13. Ragone plot of this work compare to others.

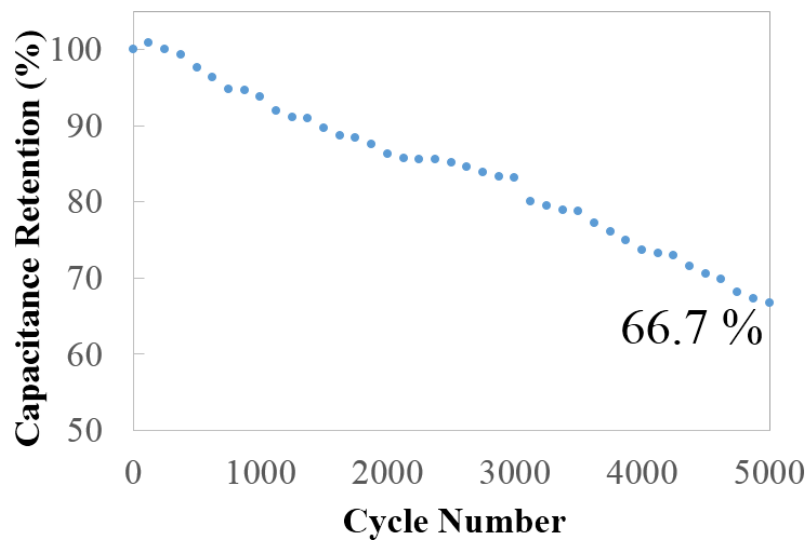


Fig. S14. Retention performance at 1 A/g of  $\text{MnO}_2/\text{ECNFs}$  under 4 h electrodeposition.

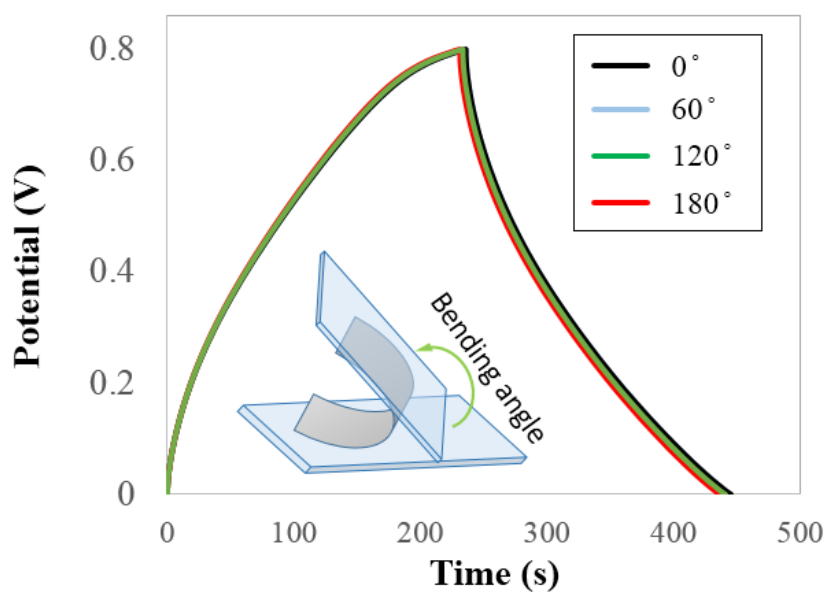


Fig. S15. Charge-discharge with folding with 0° (original), 60°, 120°, 180°, respectively.

Time(h)	Mass (mg)	Dev. (mg)
0.5	0.04	±0.02
1	0.09	±0.05
1.5	0.15	±0.09
2	0.23	±0.10
2.5	0.32	±0.11
3	0.43	±0.14
3.5	0.49	±0.13
4	0.52	±0.16

Table S1. Mass loading of MnO<sub>2</sub> on ECNFs at deposition time from 0.5 to 4 h.

## SUPPORTING REFERNCES

1. Zhang, L., Aboagye, A., Kelkar, A., Lai, C., & Fong, H. (2014). A review: carbon nanofibers from electrospun polyacrylonitrile and their applications. *Journal of Materials Science*, 49(2), 463-480.
2. Yu, G., Hu, L., Liu, N., Wang, H., Vosgueritchian, M., Yang, Y., & Bao, Z. (2011). Enhancing the supercapacitor performance of graphene/MnO<sub>2</sub> nanostructured electrodes by conductive wrapping. *Nano letters*, 11(10), 4438-4442.
3. Zhang, L. L., & Zhao, X. S. (2009). Carbon-based materials as supercapacitor electrodes. *Chemical Society Reviews*, 38(9), 2520-2531.